Cancer Research

[^{18}F](2*S*,4*R*)4-Fluoroglutamine PET Detects Glutamine Pool Size Changes in Triple-Negative Breast Cancer in Response to Glutaminase Inhibition

Rong Zhou, Austin R. Pantel, Shihong Li, Brian P. Lieberman, Karl Ploessl, Hoon Choi, Eric Blankemeyer, Hsiaoju Lee, Hank F. Kung, Robert H. Mach, and David A. Mankoff

Abstract

Glutaminolysis is a metabolic pathway adapted by many aggressive cancers, including triple-negative breast cancers (TNBC), to utilize glutamine for survival and growth. In this study, we examined the utility of [^{18}F](2S,4R)4-fluoroglutamine ([^{18}F]4F-Gln) PET to measure tumor cellular glutamine pool size, whose change might reveal the pharmacodynamic (PD) effect of drugs targeting this cancer-specific metabolic pathway. High glutaminase (GLS) activity in TNBC tumors resulted in low cellular glutamine pool size assayed via high-resolution ^{1}H magnetic resonance spectroscopy (MRS). GLS inhibition significantly increased glutamine pool size in TNBC tumors. MCF-7 tumors, with inherently low GLS activity compared with TNBC, displayed a larger baseline glutamine pool size that did not change as much in response to GLS inhibition. The tumor-to-blood-activity ratios (T/B) obtained from [^{18}F]4F-Gln PET images matched the distinct glutamine pool sizes of both tumor models at baseline. After a short course of GLS inhibitor treatment, the T/B values increased significantly in TNBC, but did not change in MCF-7 tumors. Across both tumor types and after GLS inhibitor or vehicle treatment, we observed a strong positive correlation between T/B values and tumor glutamine pool size measured using MRS ($r^2 = 0.71$). In conclusion, [^{18}F]4F-Gln PET tracked cellular glutamine pool size in breast cancers with differential GLS activity and detected increases in cellular glutamine pool size induced by GLS inhibitors. This study accomplished the first necessary step toward validating [^{18}F]4F-Gln PET as a PD marker for GLS-targeting drugs. *Cancer Res; 77(6); 1476–84. ©2017 AACR.*

Introduction

Glutamine (Gln) is the most abundant amino acid in the blood. In addition to participating in cellular protein synthesis, Gln is a substrate in the glutaminolysis pathway (diagram in Fig. 1), which is highly active in many aggressive forms of human cancers, including triple-negative breast cancer (TNBC), glioma, lymphoma, pancreatic, and lung cancers (1–7). The first and rate-limiting step of glutaminolysis is catalyzed by mitochondrial glutaminase (*GLS*), which converts Gln to glutamate. Glutamate can then be used to fuel the tricarboxylic acid (TCA) cycle, from which intermediates (e.g., citrate) can be exported and used in biosynthesis (e.g., of lipid for cell membrane). By activating glutaminolysis, cancers are able to utilize both glycolysis (the Warburg effect) and the TCA cycle to fulfill their demands for energy and biosynthesis. Consequently, cancers with active glutaminolysis may become "addicted" to Gln for growth and proliferation (8–11). To exploit this tumor-specific metabolic alteration, small-molecule inhibitors targeting Gln metabolism have been developed (12–16). Candidates that inhibit the rate-limiting enzyme, *GLS*, have shown promising results in preclinical studies of solid tumors including TNBC (1, 2). Some have advanced to clinical trials (e.g., NCT02071862; ref. 17). However, clinical laboratory tools have not been developed to identify patients whose tumors might benefit from *GLS*-targeted therapy or measure the pharmacodynamic (PD) effect of *GLS*-inhibiting drugs. This would not only require tissue biopsy, but also the ability to maintain the enzyme-inhibitor binding status during assay process. A noninvasive *in vivo* imaging marker capable of assessing glutaminolysis and the PD effect of *GLS* inhibitors could overcome these limitations and guide early drug trials.

The fluorine-18–labeled Gln analogue, [^{18}F](2*S*,4*R*)4-Fluoroglutamine ([^{18}F]4F-Gln), detectable by PET, has recently been developed to study Gln transport and kinetics (18, 19). Based on an earlier report that this Gln analogue is taken up by cells via the same transporters as Gln (20), but is minimally metabolized in tumor cells (19, 21), we performed studies to test the feasibility of using [^{18}F]4F-Gln PET to measure changes in cellular Gln pool size in response to *GLS* inhibition in breast cancers. We chose to use two breast cancer models with distinct *GLS* activities: TNBC exhibiting high *GLS* activity and estrogen receptor positive (ER^{+}) breast cancer with inherently low *GLS* activity (1). This feasibility study is the first necessary step toward establishing [^{18}F]4F-Gln PET as a PD marker of drugs targeting glutaminolysis.

Department of Radiology, University of Pennsylvania, Philadelphia, Pennsylvania.

Note: Supplementary data for this article are available at Cancer Research Online (http://cancerres.aacrjournals.org/).

Corresponding Authors: Rong Zhou, University of Pennsylvania, 198 John Morgan, Philadelphia, PA 19104. Phone: 215-746-8747; Fax: 215-573-2255; E-mail: rongzhou@upenn.edu; or David A. Mankoff, david.mankoff@uphs.upenn.edu

doi: 10.1158/0008-5472.CAN-16-1945

AACR

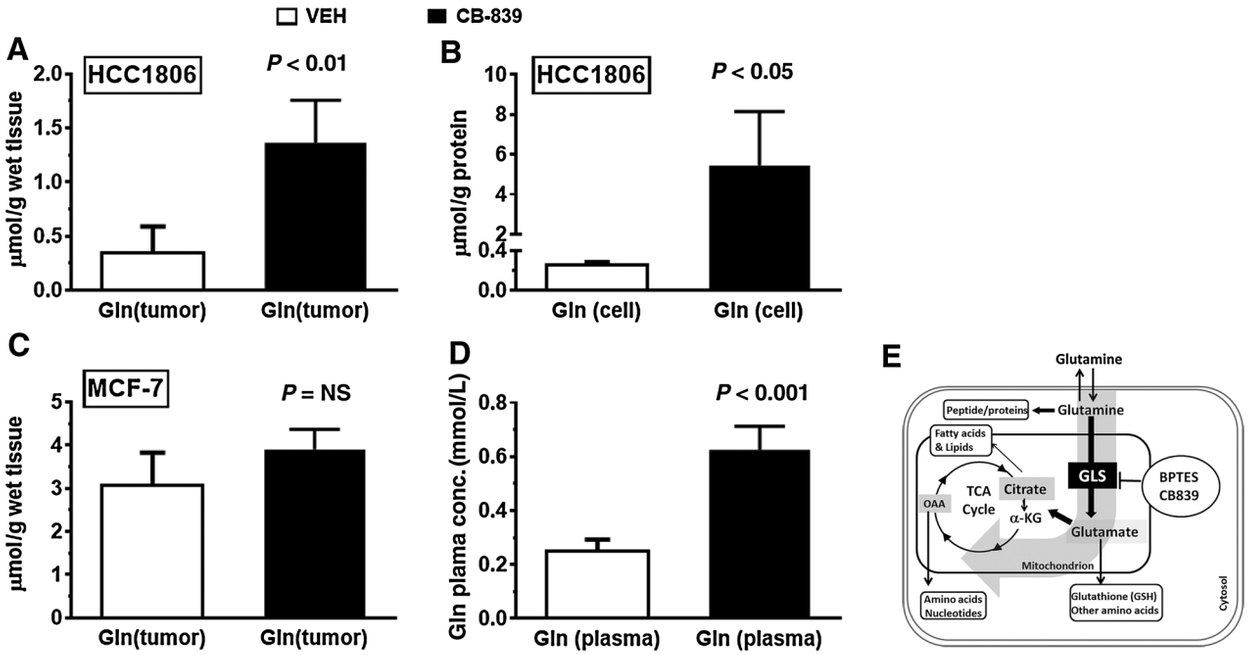

Figure 1.

Tumor tissue and cellular Gln concentration after CB839 or vehicle treatment. **A,** Gln concentration (μmol/g of tissue wet weight) in TNBC tumors after 4 to 6 doses of CB839 ($n = 4$) or VEH ($n = 4$) treatment. **B,** Gln concentration (μmol/g of protein) in HCC1806 cells after 24-hour incubation with culture media containing 1 μmol/L CB839 or VEH ($n = 2$ for each group). **C,** Gln concentration in MCF-7 tumors after 4 to 6 doses of CB839 ($n = 4$) or VEH ($n = 3$) treatment ($P = 0.07$). **D,** Plasma Gln concentration in CB839-treated ($n = 4$) or VEH-treated ($n = 4$) mice (pooled from mice bearing HCC1806 or MCF-7 tumors). NS, not significant. **E,** Diagram of cancer-specific glutaminolysis pathway (gray arrow), in which the first and rate-limiting step catalyzed by *GLS* is inhibited by small-molecule drugs including BPTES and CB839.

Materials and Methods

Human TNBC (HCC1806 and HCC38) and ER$^+$ (MCF-7) breast cancer cell lines purchased from the ATCC over the span of 2012 to 2016 were authenticated by the cell bank using the short tandem repeat DNA profiling method and were passaged less than 6 months after resuscitation. Cells were maintained in complete culture media consisting of RPMI 1640 supplemented with 10% FBS (no antibiotics were used). These lines were chosen based on the distinct *GLS* activities reported previously (1) and confirmed in our study: 35 to 55 nmol/min/mg protein in the TNBC lines versus 5 nmol/min/mg protein in MCF-7. Radiosynthesis of [^{18}F]4F-Gln followed previously established methods (18, 22). The minimum specific activity of [^{18}F]4F-Gln at the end of synthesis was 40 mCi/μmol, and the maximal molar dose was 8.75 nanomoles based on the injected dose specified below. Two *GLS* inhibitors were examined in this study: BPTES (bis-2-(5-phenylacetamido-1,2,4-thiadiazol-2-yl)ethyl sulfide) (13) was purchased (Sigma) and CB839 (1) was supplied by Calithera, Inc. via a material transfer agreement between institutes.

In vitro cell uptake of [^{18}F]4F-Gln

HCC1806 (25,000 cells/well) and MCF-7 (30,000 cells/well) were attached to a 96-well plate overnight. CB839 stock solution (10 mmol/L in DMSO) was serially diluted in complete media to 1 μmol/L (final DMSO concentration was 0.05%) and incubated with cells for 4 hours. Control cells were incubated in media containing 0.05% DMSO. To study tracer uptake, the culture media were replaced by PBS (with Ca^{++} and Mg^{++} to facilitate normal cell functions such as uptake and attachment) containing 5 mmol/L glucose, 100 μmol/L *L*-Gln (Sigma), 1 μmol/L CB839 (or 0.05% DMSO), plus [^{18}F]4F-Gln ligand (~300,000 cpm/well in nano- to pico-molar concentration). At specified time points (5, 15, 30, 60, and 120 minutes), supernatant was aspirated and the wells were washed twice with cold PBS (without Ca^{++} and Mg^{++}). Samples are counted on the gamma counter (2470 WIZARD2; Perkin Elmer), and the amount of protein per well was estimated by the Lowry method. Of note, owing to reversible nature of *GLS* inhibition mediated by CB839, the drug was present during tracer uptake period. The concentration of cold *L*-Gln was optimized to 100 μmol/L so that it did not block [^{18}F]4F-Gln uptake while preventing the tracer from being depleted during the 2-hour uptake study.

Tumor implantation and treatment

All animal studies were approved by the animal care and usage committee (IACUC) of the University of Pennsylvania.

Xenografts from HCC1806, HCC38, and MCF-7 were established in NCR athymic nu/nu mice (female, 7 weeks old; Charles River) as we described previously (23). Only one type of cell was implanted in a single location in each mouse (the flank). Briefly, 1 million HCC1806 cells in PBS, 10 million HCC38 cells in Matrigel (1:1 mixed with PBS), or 5 million MCF-7 cells in Matrigel were implanted subcutaneously in the flank of the mouse. One week before MCF-7 cells' implantation, a 60-day-release tablet containing 17β-estradiol (Innovative Research America) was implanted under the skin of the neck region. Compared with HCC38,

HCC1806 xenografts grew more robustly. Although both were used in this study, the majority of the data presented in Results section were from HCC1806.

We examined two highly selective, potent, and reversible inhibitors of *GLS* in this study. BPTES was used to treat the TNBC (HCC1806) model in a pilot study, whereas CB839 was used to treat both the TNBC and MCF-7 models in subsequent studies. BPTES (dissolved in DMSO and diluted in saline to the final concentration of 0.8 mg/mL containing 4% DMSO) was administered via intraperitoneal injection at 12.5 mg/kg/day for 6 days. CB839, dissolved in the vehicle solution (VEH) of 25% (w/v) hydroxypropyl-β-cyclodextrin in 10 mmol/L citrate (pH 2), was administered via oral gavage (200 mg/kg twice daily); control mice received the same volume (0.25 mL) of VEH. A total of 4 to 6 doses (2–3 days) of CB839 or VEH were administered. Because CB839 has fast clearance and its inhibitory effect on GLS is slowly reversible (1), this short treatment course ensured tumor exposure to the drug, without causing substantial changes in tumor volume.

HPLC-based analysis of [^{18}F]4F-Gln metabolites

After four doses of CB839 or VEH treatment, mice were injected with [^{18}F]4F-Gln (same activity as for imaging—see below). One hour after injection, the tumor was harvested and the blood was collected via cardiac puncture. All samples were kept on ice during processing. The plasma was obtained by centrifuging the blood (3,000 *g* for 10 minutes at 4°C) and was mixed with 1 mL acetonitrile (ACN). The mixture was vortexed thoroughly and then followed by another round of centrifugation (3,000 *g* for 10 minutes at 4°C). The supernatant and the pellet were separated and counted with a gamma counter (2480 series; Perkin Elmer) to determine the extraction efficiency. Part of the supernatant (>200 μL) was then filtered with a 0.45 μm filter, and 200 μL of the filtered supernatant was injected into an analytical metabolite HPLC (1200 series; Agilent Technologies) equipped with an Astec CHIROBIOTIC T Chiral HPLC column (5 μm, 25 cm × 4.6 mm; Sigma-Aldrich) and a fraction collector (Waters). The mobile phase consisted of 80:20 methanol:water (v/v), and the flow rate was 1 mL/min. A fraction was collected every 30 seconds and counted with the Perkin Elmer gamma counter. The activity in each fraction was then plotted against the fraction number. The areas under the curve from each peak were summed to determine the percentage of activity from the parent ligand ([^{18}F]4F-Gln) versus metabolite(s). Fractions #9 to #14 represented the parent ligand ([^{18}F]4F-Gln) as validated by HPLC analysis of the cold compound; all other peaks were considered as metabolites. Our HPLC method can separate [^{18}F]4F-Gln versus [^{18}F]4F-glutamate (Supplementary Fig. S1). The latter was part of the "metabolites" fraction reported in our study.

For HPLC analysis of tumor tissue, the tumor tissue was first homogenized in 1 mL ice-cold PBS. Subsequently, 1 mL ice-cold denaturing solution (3:1 ACN: water v:v) was added to denature the proteins, and the mixture was vortexed. The supernatant and pellet were separated by centrifugation (3,000 *g* for 10 minutes at 4°C) and were counted. The filtration of supernatant and HPLC analyses followed the same protocol for plasma as detailed above.

In vivo PET studies and image analysis

Each mouse underwent pre- and posttreatment PET scans. PET studies were performed on a dedicated small animal scanner (A-PET). Technical details of the A-PET are similar to the commercial Mosaic HP scanner from Philips Healthcare as described before (24). Briefly, the scanner uses 2 mm × 2 mm × 10 mm lutetium (yttrium) orthosilicate (LYSO) crystals with 2.3-mm pitch, resulting in a transverse spatial resolution of 2.3 mm and axial spatial resolution of 2.4 mm. The detector diameter is 19.7 cm with a length of 11.6 cm. The latter allows the field-of-view to encompass the whole mouse, including the tail. The system is fully three dimensional (3D), without interplane septa. Images were reconstructed with the 3D row action maximum likelihood algorithm (3D RAMLA; ref. 25) into 1 mm^3 isotropic resolution. Random subtraction and decay correction were applied; scatter and attenuation correction were not used. During imaging, the mouse was sedated by 1 L/min oxygen containing 1.5% isoflurane via a nose cone and prone on a heating pad.

Dynamic PET scans were used for a pilot study—to determine the optimal imaging time for uptake measures for subsequent studies. Each scan was started immediately after tracer (300–350 μCi) injection with a temporal resolution of 5 min/frame × 12 frames for 1 hour of imaging. PET images were analyzed using AMIDE software (http://amide.sourceforge.net/). To measure blood activity, an ROI of fixed size (2 × 2 × 2 mm^3 box) was placed on the anatomical location of the heart, noting that tracer accumulation in myocardium did not exceed blood pool background. For tumors, a single spherical ROI with a volume of $^1/_8$ (12.5%) the size of the tumor volume as measured by calipers prior to the PET scan was centered on the tumor area with maximal uptake. This approach is akin to the "peak" ROI used in clinical PET analysis (26). Other single ROI methods ($^1/_4$ and $^1/_2$ of caliper-based tumor volume) were also examined as detailed in Supplementary Information. In such cases, the ROI often covered portions of tumor with low tracer uptake (nonviable or cystic tumor). Time-activity curves (TAC) of the blood and tumor were constructed as T/B or %ID/g, calculated from the Eq. A, where WM_ROI was the ROI enclosing the whole mouse.

$$\%\mathrm{ID/g} = \frac{\mathrm{tumor\_ROI\_mean\_counts} \times \mathrm{tumor\_ROI\_volume}}{[\mathrm{WM\_ROI\_mean\_counts} \times \mathrm{WM\_ROI\_volume}]} \times \frac{1}{\mathrm{tumor\_ROI\_volume} \times 1\ \mathrm{g/cm^3}} \times \frac{1{,}000\ \mathrm{mm^3}}{\mathrm{cm^3}} \times 100\% \quad \text{(A)}$$

TACs of T/B revealed a time window of 30 to 45 minutes after injection when the T/B reached equilibrium. In subsequent studies using CB839, a static 15-minute PET scan protocol, starting at 30 minutes after [^{18}F]4F-Gln injection, was applied, and T/B values estimated from static PET images were used to estimate tumor Gln pool size. The posttreatment scan was timed at 4 hours after the last gavage of CB839 to ensure the absorption of the drug.

Because the whole tumor homogenate was used for MRS-based Gln pool size measurement (see section below), we also estimated T/B value from the entire tumor using a multiROI approach in which planar ROIs were manually defined on each image slice to cover the whole tumor (detailed procedure described in Supplementary Information).

^{1}H MR spectroscopy quantification of tumor Gln pool size from tumor extracts

Gln concentration in cell, tumor, and blood samples was estimated by ^{1}H magnetic resonance spectroscopy (MRS) of aqueous metabolite extraction. After HCC1806 or MCF-7 cells

were incubated with 1 μmol/L CB839 or 0.05% DMSO in culture media for 24 hours, cell pellet (from ~10^7 cells) was collected by centrifuge (1,000 *g* for 10 minutes). Methanol:water (1:1 v:v total 500 μL per pellet) was added, and metabolites were extracted in the aqueous phase (27). The protein content of the cell pellet was estimated by the Lowry method. The extracted sample was then lyophilized and prepared for MRS analysis in the same manner as for tumors described below.

After posttreatment PET imaging, the whole tumor was harvested and freeze-clamped between a pair of aluminum tongs, which were precooled in liquid nitrogen and stored at −80°C until extraction. The blood was collected via cardiac puncture under deep anesthesia. Plasma was separated from blood and was extracted in a similar fashion as cells. To extract soluble metabolites from the tumor, the sample was first weighed (the weight ranges from 0.14–0.74 g) and then pulverized in liquid nitrogen using a suitable size mortar/pestle. Perchloric acid (PCA, 6.6%) was added at 3 mL per gram of tissue to the pulverized sample, which was thawed and homogenized followed by centrifugation (11,000 *g* for 20 minutes at 4°C). The pH of the supernatant was adjusted to 7.0 ± 0.2, using KOH and PCA in graded concentrations. The precipitated potassium perchlorate was removed by centrifugation (1,000 *g* for 10 minutes at 4°C). The sample was then lyophilized and stored at −80°C freezer.

For high-resolution ^{1}H MRS, the lyophilized powder was dissolved in 0.5 mL D_2O and filtered into a 5-mm (diameter) NMR tube. A glass capillary containing trimethylsilyl propanoic acid reference solution was calibrated inside the NMR tube to be 0.408 mmol/L. ^{1}H MRS was performed on a 400 MHz vertical bore spectrometer (Avance DMX 400; Bruker Instruments Inc.) using a 5-mm radiofrequency coil. ^{1}H MR spectra were analyzed by NUTS software (Acorn NMR) with the reference peak set at 0 ppm. The integration of a metabolite peak(s) in an MR spectrum is proportional to its concentration. To determine the Gln concentration in the NMR tube, the integrated Gln-H4 resonance peaks (at 2.48–2.42 ppm) relative to the reference peak were multiplied by 0.408 mmol/L. Multiplying the Gln concentration by sample volume (0.5 mL) gave the amount of Gln in the sample. The amount of Gln was normalized to the tissue wet weight, total protein in the cell pellet, and plasma volume, yielding Gln concentration in the tumor tissue (μmol/g), tumor cells (μmol/g of protein), and plasma (μmol/mL), respectively. In spectra obtained from the 400 MHz MR spectrometer, there was no overlap of Gln-H4 peaks with glutamate-H4 peaks or with other metabolites at the detection sensitivity of MRS, assuring no contamination in the Gln pool size estimation.

Data are presented as mean ± SEM unless otherwise noted. Statistical tests were performed using GraphPad Prism 6. Two-sided Student *t* tests were used to evaluate significance at the $\alpha = 0.05$ level. To examine correlation, the squared Pearson correlation coefficient (r^2) was calculated in GraphPad Prism 6 or Excel.

Results

Change of Gln concentration (pool size) in cells, tumors, and plasma in response to GLS blockade

^{1}H MRS quantification revealed that after a short course (2–3 days) of CB839 treatment, Gln concentration in TNBC (HCC1806) tumor extracts increased from 0.31 ± 0.10 μmol/g after VEH treatment to 1.35 ±0.20 μmol/g after CB839 treatment, a 4.3-fold increase ($P = 0.007$; Fig. 1A). The invasive nature of the MRS assay did not allow pre- versus posttreatment comparison; instead, samples from CB839-treated mice were compared with VEH-treated ones as controls (without *GLS* inhibition). This increase of cellular Gln pool is the most immediate metabolic consequence of *GLS* inhibition (Fig. 1E). In HCC1806 cells taken from culture, the increase of cellular Gln pool size induced by *GLS* inhibitor was even more dramatic (>20-fold; Fig. 1B). In contrast, the MCF-7 tumors exhibited a higher Gln concentration without *GLS* inhibition (3.08 ± 0.390 μmol/g) and a moderate increase afterward (3.90 ± 0.23 μmol/g, $P > 0.05$; Fig. 1C). After CB839 treatment, the plasma Gln concentrations were similar in TNBC or MCF-7–bearing mice (both from the same strain); therefore, the data were pooled into CB839 and VEH groups without discriminating tumor models: the plasma Gln concentration was 0.62 ± 0.04 mmol/L after CB839 compared with 0.25 ± 0.02 mmol/L after VEH treatment (~2.5-fold increase; Fig. 1D; $P < 0.001$).

Cellular uptake of [^{18}F]4F-Gln in response to GLS blockade

The initial uptake (up to 30 min) of [^{18}F]4F-Gln into TNBC and MCF-7 cells was similar in the presence of CB839 versus DMSO, suggesting that the Gln transporter activities were not blocked by *GLS* inhibitor. For the HCC1806 cells, tracer uptake plateaued at a higher level after *GLS* inhibition compared with DMSO-treated cells ($P < 0.001$): the tracer uptake in CB839-treated cells was > 3-fold of VEH-treated cells at 60 minutes, and >2-fold at 120 minutes (both $P < 0.0001$; Fig. 2A). The reduced [^{18}F]4F-Gln activity in DMSO-treated HCC1806 cells at later time points (60–120 min) was consistent with tracer efflux corresponding to a small Gln pool size due to *GLS* activity (Fig. 1B). Compared with HCC1806 cells, [^{18}F]4F-Gln uptake in MCF-7 cells were higher without *GLS* inhibition, and CB839 treatment induced a much smaller increase in tracer accumulation (Fig. 2B).

Lack of significant metabolic conversion of [^{18}F]4F-Gln in tumors and blood

Centrifugation of tumor homogenates led to 90% ± 1% ($n = 12$) of the activity in the supernatant while 10% ± 1% ($n = 12$) in the pellet, suggesting minimal tracer incorporation into macromolecules. We compared different methods in our pilot studies to denature and precipitate proteins: ACN/water (used here) or ACN combined with trichloroacetic acid (10%), and the results (% activity in pellet) were almost identical (data not shown), suggesting that ACN/water can efficiently denature proteins to release small molecules while it does not require adjusting pH of the supernatant. HPLC analysis of supernatant revealed the parent ligand was the dominant species accounting for ≥85% of the total activity, similar in both tumor type and treatment groups, whereas 9% to 14% of activity was summed from other peaks in the HPLC profile (Fig. 3A).

Total blood activity was divided between blood cells & platelets (37% ± 4%, $n = 6$) and plasma (63% ± 4%, $n = 6$). In plasma samples, 25% ± 4% of the activity was found in the pellet, whereas 75% ± 4% was found in the supernatant ($n = 6$). HPLC analysis of the supernatant suggested that the majority (82%–87%) of activity was from the parent ligand and a small fraction (≤16%) was from metabolites (Fig. 3B). Findings in Fig. 3 confirmed that [^{18}F]4F-Gln was the primary species in the tumor and blood. The modest amount of labeled metabolites seen in the blood, and an even smaller average metabolite fraction in the

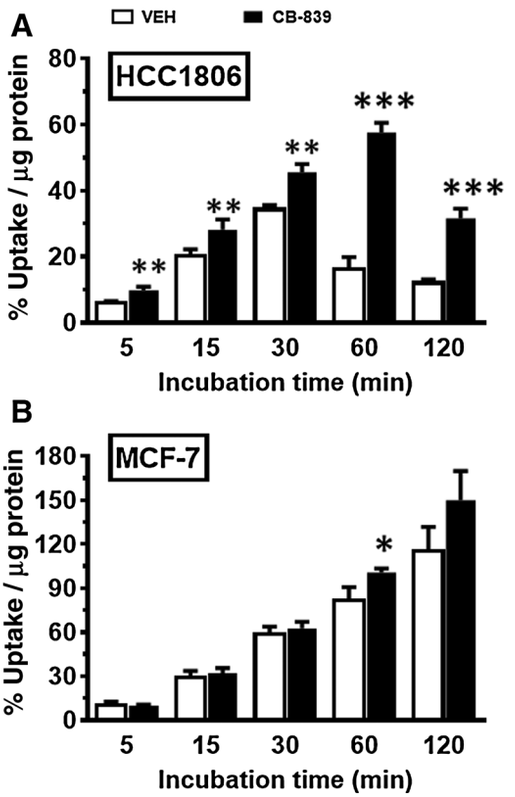

Figure 2.
Cell uptake of [^{18}F]4F-Gln tracer over incubation time. **A,** Tracer uptake in HCC1806 cells that were incubated for 4 hours with CB839 ($n = 4$ for each time point) or VEH ($n = 4$ for each time point). **B,** Tracer uptake in MCF-7 cells (the same sample size as in **A**). CB839 (black) or VEH (white). *, $P < 0.05$; **, $P < 0.001$; ***, $P < 0.0001$.

tumor, suggests that the contribution of labeled metabolites to the tumor PET signal was small and unlikely to have a significant influence on image-derived measures such as the tumor-to-blood-activity (T/B) ratio. This should be further addressed in future studies examining kinetics of [^{18}F]4F-Gln uptake in tumors.

In vivo [^{18}F]4F-Gln PET detects tumors with distinct Gln pool size

In our pilot study (described in Fig. 4), we treated TNBC model with a commercially available *GLS* inhibitor, BPTES, or VEH ($n = 3$ for each group), and performed 1-hour dynamic scans. In a BPTES-treated mouse, a clear difference in TAC of the tumor relative to the blood at baseline (Fig. 4A) versus after treatment was observed (Fig. 4B). T/B ratios increased after treatment with BPTES (Fig. 4C), but were decreased in a VEH-treated mouse compared with pretreatment (Fig. 4D). Complete pre- and post-treatment [^{18}F]4F-Gln PET data sets were obtained from 2 (of 3) BPTES-treated and 1 (of 3) VEH-treated mice. From these data sets, we were able to identify a time window (30–45 minutes after tracer injection) during which tumor uptake and blood clearance of the tracer reached approximate steady state. T/B values obtained from this window (between the red lines in Fig. 4B) revealed a 51% increase over baseline in one and 8% increase in the other BPTES-treated mouse, whereas an 18% decrease was observed in the VEH-treated mouse.

Visual assessment of the images agreed with numerical values: HCC1806 tumors (arrows) were less visible in baseline PET images, but showed more prominent uptake after BPTES treatment (Fig. 4E, both images were windowed at 10% ID/g, detailed in Supplementary Methods). Robust FDG uptake was observed in both pre- and post-BPTES PET images (Fig. 4F), suggesting FDG is not a PD marker of *GLS* inhibition, as expected. This pilot study was used to devise a short static PET scan protocol (15 minutes) for the subsequent studies described below.

To further test the utility of [^{18}F]4F-Gln PET for detecting changes of Gln pool size, we treated the mice with CB839, a potent *GLS* inhibitor currently being evaluated in clinical trials. After a short treatment course (2–3 days), mice underwent a 15-minute PET scan starting at 30 minutes after tracer injection. In TNBC-bearing mice, although T/B values exhibited some variation at baseline, T/B values increased in all CB839-treated mice ($P < 0.05$ using two-tailed paired t test) and decreased in 3 out of 4 VEH-treated mice (Fig. 5A, left panel). In receptor-positive MCF-7 tumors, pretreatment T/B values were higher compared with TNBC tumors ($P < 0.05$, t test of the mean without assumption of equal variance), and changes in T/B values after CB839 versus VEH treatment were not significant (Fig. 5A, right panel). Similar to

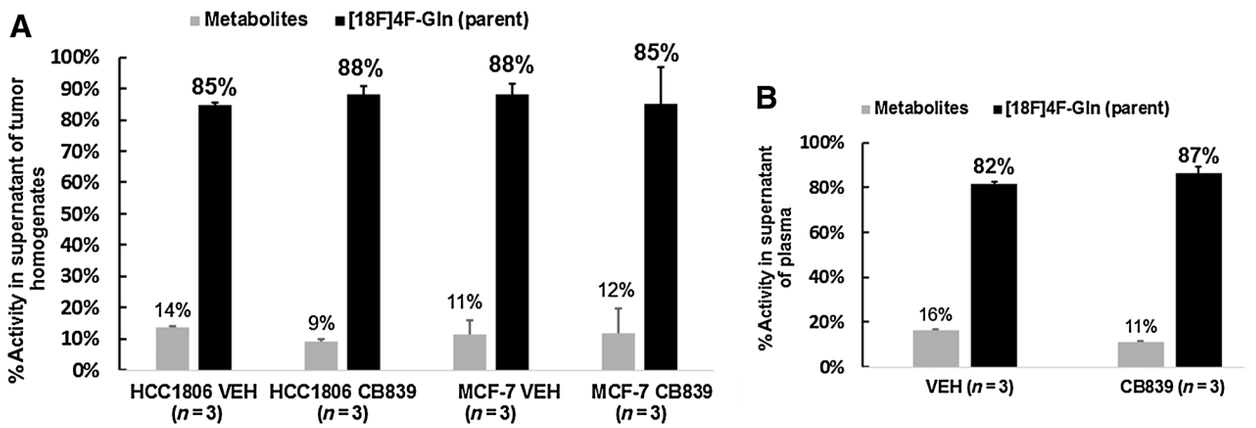

Figure 3.
Lack of significant metabolic conversion of [^{18}F]4F-Gln in the tumor and blood. The fraction of radioactivity from the parent ligand vs. metabolites in the supernatant of protein-denatured homogenates of tumor tissue (**A**; $n = 3$ for each group) and in the supernatant of protein-denatured plasma samples (**B**; $n = 3$ for each group).

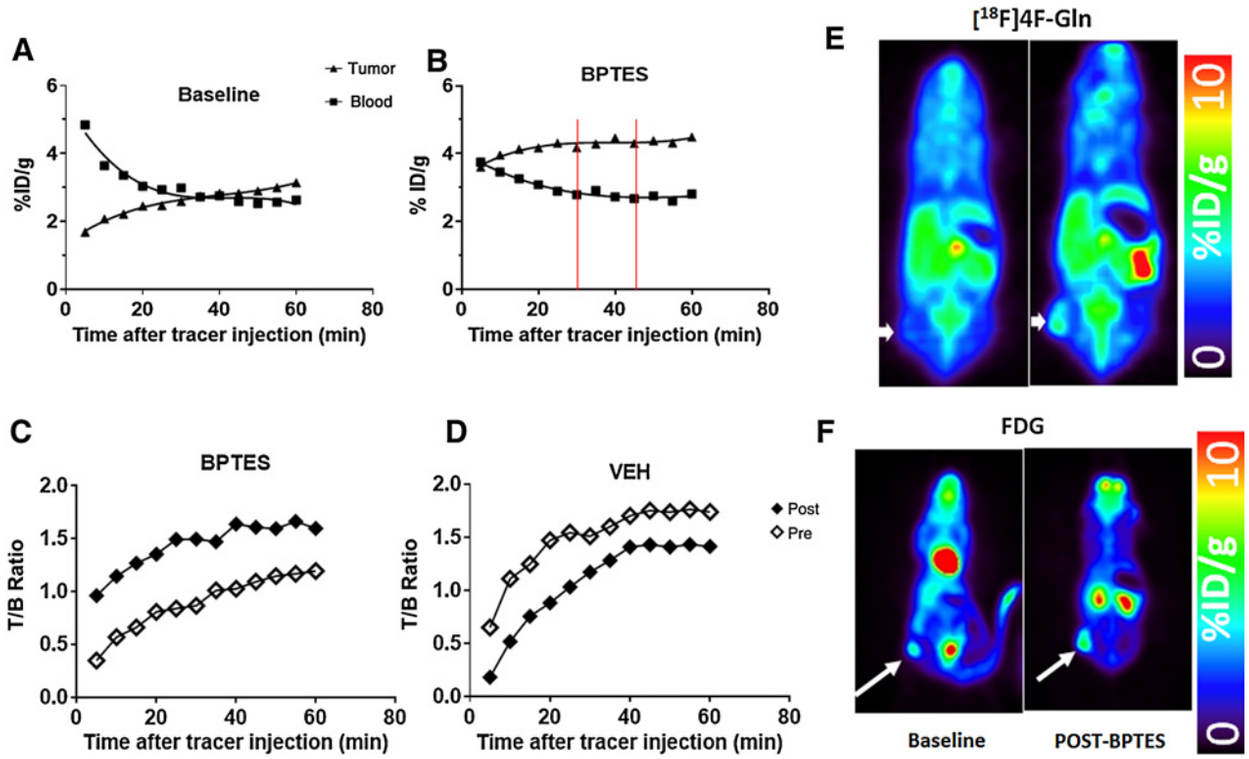

Figure 4.

Kinetic study to derive T/B time course in TNBC-bearing mice treated with GLS inhibitor BPTES. **A** and **B,** Time-activity curves of the blood and tumor from a single mouse at baseline (**A**) and after 6 daily treatments of BPTES (**B**). **C** and **D,** T/B time course obtained from pre- and posttreatment PET images was plotted for the same BPTES-treated mouse as in **A** and **B** and a VEH-treated mouse. Note the relative position of pre- and posttreatment T/B time courses was reversed in BPTES compared with VEH-treated mouse. **E,** PET images summed from 30 to 45 minutes of dynamic scan and registered to the similar anatomical plane revealed the markedly enhanced conspicuity of the tumor after BPTES treatment. **F,** Robust FDG uptake at baseline and post-BPTES treatment. Arrows in **E** and **F**, tumors. Red lines in **B** defined a time period (30–45 min) when the tracer uptake and clearance became steady state. In this pilot study, each group was started with 3 mice; complete data sets (baseline and after treatment) were obtained from 2 mice in BPTES group and 1 mouse in VEH group.

BPTES treatment, HCC1806 tumors exhibited enhanced [^{18}F]4F-Gln PET signal on the post-CB839 images compared with pre-treatment (Fig. 5B, top). In contrast, MCF-7 tumors showed strong [^{18}F]4F-Gln PET signals on both pre- and post-CB839 treatment images (Fig. 5B, bottom). In TNBC tumors, T/B value increased 34% ± 7% after CB839 treatment in comparison with an 11(±12)% decrease after VEH treatment ($P < 0.05$, t test of the mean percent change, without assumption of equal variance, Fig. 5C, left). Notably, the increase of T/B induced by CB839 treatment was accompanied by a 6(±7)% decrease in tumor size, whereas the T/B decrease after VEH treatment was accompanied by a 35(±20)% increase in tumor size (Fig. 5C, right), suggesting that the changes in T/B after CB839 or VEH treatment were not due to partial volume effect resulting from small tumor size or change in tumor size after treatment.

We next examined the correlation between T/B values obtained from posttreatment PET images versus Gln pool size measured from the same tumors (which were harvested after imaging). We identified a strong correlation (Fig. 5D; $r^2 = 0.71$, $P = 0.0002$), where T/B values obtained using the multiROI method (Supplementary Information). When T/B values from single ROI ($^1/_8$ of caliper size) method were used, r^2 was 0.44. This suggests that the multiROI method might better account for the heterogeneity of the tumor, leading to a stronger correlation, noting that MRS-based Gln pool size estimates used extracts from homogenates of the entire tumor.

To evaluate whether the image analysis methods were robust to different readers or the usage of different sized tumor ROIs, we compared T/B values obtained by two readers and from various ROI methods ($^1/_8$, $^1/_4$, and $^1/_2$ of caliper size or multiROI). In the single ROI methods, the ROI size was proportional to caliper-based tumor volume. This approach reduced the impact of tumor size variations on T/B measurements and appeared to be robust to different readers or ROI size; the T/B values obtained from the two readers were highly correlated ($r^2 = 0.99$; Supplementary Fig. S2). Strong correlations were also observed between single ROI of different sizes ($^1/_8$ vs. $^1/_4$ or $^1/_2$ of caliper size; $r^2 \geq 0.94$; Supplementary Fig. S3). The correlation between the single ROI ($^1/_8$ caliper) versus multiROI method was still strong, but slightly lower ($r^2 = 0.80$; Supplementary Fig. S4). As the latter covered the entire tumor, it likely averaged across the heterogeneous PET signals from portions of the tumor that were viable, cystic, or necrotic; such heterogeneity was most notable in TNBC model and visualized in the PET images (e.g., Fig. 5B, top).

Because T/B index represents an approximation of tracer's cellular distribution volume fraction (DV), we also estimated DV by analyzing the dynamic PET images (Supplementary Fig. S5A) with the Logan graphical method and two-compartment

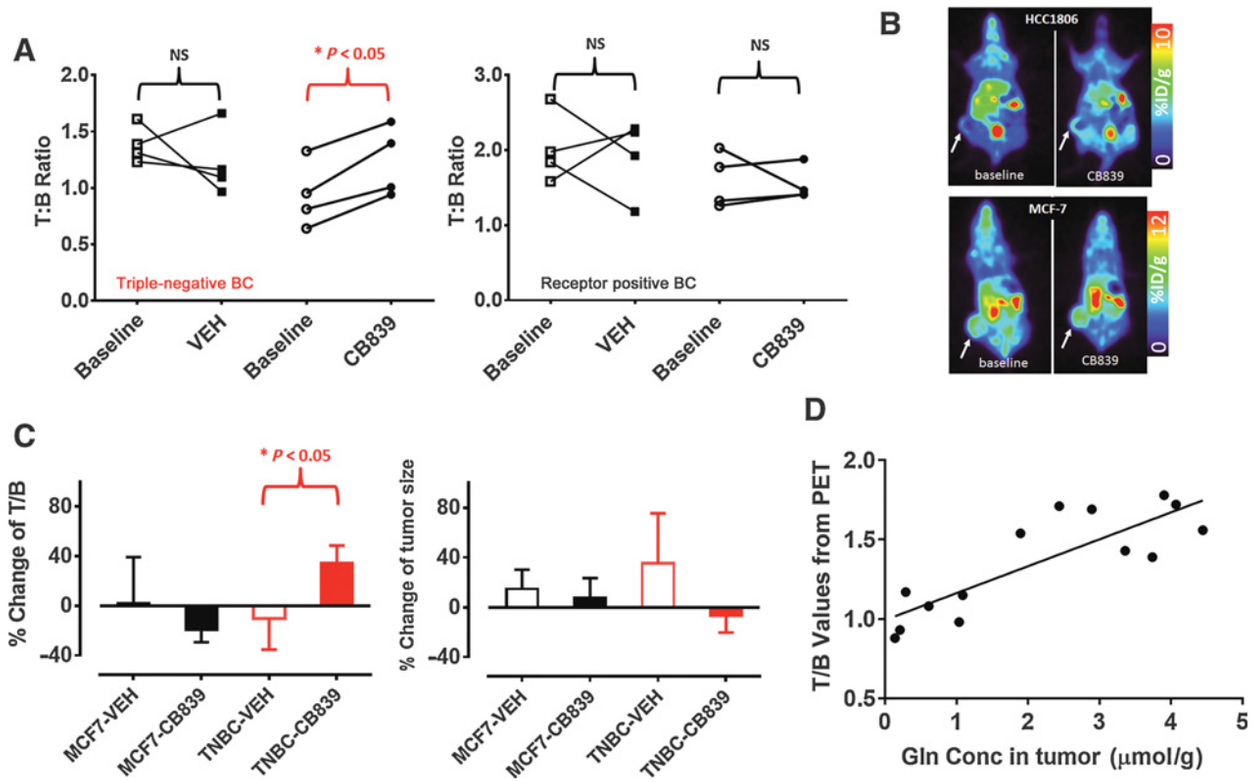

Figure 5.

T/B estimated from [^{18}F]4F-Gln PET tracks tumor Gln pool and its change induced by CB839. **A,** Pre and posttreatment T/B values from TNBC and MCF-7 tumors reveal their differential responses to *GLS* inhibition ($n = 4$ for each group). **B,** PET images are shown for a mouse bearing HCC1806 and one bearing MCF-7 tumor scanned before and after CB839 treatment. Note a maximal color scale of 12%ID/g used for MCF-7 tumors while 10%ID/g was used for TNBC tumor (detailed in Supplementary Methods). **C,** Percent change of T/B value and tumor size after treatment compared with that before treatment (group size is the same as in **A**). **D,** Correlation between posttreatment T/B values (*y*-axis) versus tumor Gln concentrations (*x*-axis; $r^2 = 0.71$, $P = 0.0002$). Fourteen of 16 tumors imaged in **A** were harvested after PET imaging for MRS measurement. T/B values were obtained from the multiROI method described in Supplementary Information.

modeling (Supplementary Fig. S5B and S5C). The late linearity revealed from Logan plot (Supplementary Fig. S5B) and the small rate constant k_3 (0.008/min derived from modeling fit in Supplementary Fig. S5D) indicated minimal tracer trapping and nearly completely reversible tracer exchange between blood and tissue. This was consistent with the small fraction of activity (10%) trapped in macromolecules in the pellet of ACN-extracted tissues, and supported our hypothesis that [^{18}F]4F-Gln DV traces the cellular Gln pool. Preliminary analysis using Logan analysis showed expected changes in DV after GLS inhibition (28). This approach will provide a theoretical frame for using T/B as an index of the cellular Gln pool size, because the static imaging for deriving the T/B ratio is a clinically feasible procedure.

Discussion

TNBC represents an aggressive subtype of breast cancer. However, unlike other subtypes of breast cancer that express specific receptors such as the ER or HER2, TNBC lacks a specific target for subtype-specific therapy (29). Preclinical studies of GLS inhibitors support that inhibition of Gln metabolism might provide a therapeutic strategy for TNBC because some TNBCs exhibit high levels of *GLS* activity combined with low expression/activity of glutamine synthetase (*GLUL*; refs. 30, 31). We sought to develop a noninvasive imaging marker to identify glutaminolytic breast cancers and to measure the impact of *GLS*-targeted therapy. The overarching goal is to develop markers to help guide clinical trials and inform clinical use of Gln-targeted drugs. In this early study, our strategy was to measure cellular Gln pool size as an inverse indicator of glutaminolysis. We first demonstrated that a short course of CB839 treatment led to a significant increase of cellular Gln pool size in TNBC tumors and cultured cells (Fig. 1A and B), suggesting that an *in vivo* measure of cellular Gln pool size could be used to assess the PD effect of *GLS* inhibitors. The increase of Gln pool size in TNBC tumors after *GLS* inhibition cannot be explained by the elevated plasma Gln level following administration of the *GLS* inhibitors because (1) the increase of tumor Gln concentration (>4-fold) exceeded the increase in plasma concentration, (2) despite similar plasma Gln level increases, Gln concentration did not increase significantly in the MCF-7 tumors, and (3) in TNBC cells cultured in a standard Gln concentration, a significant increase in cellular Gln concentration was observed after CB839 treatment (Fig. 1B).

We then tested a Gln analogue, [^{18}F]4F-Gln, as a PET probe to measure cellular Gln pool size *in vivo*. For this agent to be able to trace the cellular Gln pool size, it must meet two requirements: (1) It enters and leaves the cell via Gln transporters. (2) Once in the

cell, it remains as the parent ligand (i.e., it is not metabolized). Competitive inhibition studies performed in previous studies indicated that [^{18}F]4F-Gln is transported by cellular Gln transporters including ASCT2 (SLC1A5; ref. 20). Minimal metabolism had been shown earlier (19, 21) and was confirmed in this study. Additional data from our study showed that the majority ($\geq$85%) of the radioactivity in both tumor types was from [^{18}F]4F-Gln, and this fraction was not affected by *GLS* inhibitor treatment. Furthermore, the small fraction (10%) of radioactivity trapped in the macromolecules (pellet) and the late washout of radioactive label from cultured TNBC cells suggest nearly completely reversible transport. These properties of [^{18}F]4F-Gln make it a suitable probe for tracing cellular Gln pool size.

We chose two breast cancer models that exhibit distinct levels of glutaminolysis, specifically, in the activity of the rate-limiting enzyme *GLS*: TNBC (HCC1806) was shown to have high *GLS* activity, whereas ER$^+$ (MCF-7) has low *GLS* activity. Results from these two models (Figs. 1, 2, and 5) consistently diverged along this metabolic signature, both at baseline and after treatment with *GLS* inhibitors. *In vivo* [^{18}F]4F-Gln PET results indicate that the T/B ratio can serve as an index of cellular Gln pool size. This index provides a marker for *in vivo GLS* activity and for the PD effect of *GLS* inhibitors: The high *GLS* activity in untreated TNBC tumors is associated with a small cellular Gln pool size. Thus, [^{18}F]4F-Gln competed with a small pool of *native* Gln for efflux, resulting in low tracer retention and low pretreatment T/B value. With the increase in cellular Gln pool after *GLS* inhibition, [^{18}F]4F-Gln competed with a larger pool of native Gln molecules for efflux, leading to greater retention of the radioactive tracer (and greater T/B values). Conversely, tumors with low *GLS* activity have larger Gln cellular pools at baseline—and thus higher [^{18}F]4F-Gln T/B—with minimal impact of *GLS* inhibition on probe retention.

Quantitative comparison of *in vivo* PET imaging results to MRS assay of tumor extracts provided further support for our proposed method. Comparison of posttherapy T/B values and the Gln pool sizes in both tumor models revealed a good correlation (r^2 = 0.71; Fig. 5D). Interestingly, *GLS* inhibition in TNBC induced a 1.3-fold increase of Gln pool size measured by T/B, whereas the actual Gln pool size measured by MRS increased by 4.3-fold. The underestimation of Gln pool size by T/B can be explained by competition of plasma Gln with [^{18}F]4F-Gln for cell uptake, resulting in lower T/B values when plasma Gln level is elevated. With the 2.5-fold increase in plasma Gln, the increase in T/B implies an overall $1.3 \times 2.5 = 3.3$-fold increase in Gln pool size as estimated by imaging. This compares well to the 4.3-fold actual increase in Gln pool size.

Some limitations of this study include examination of a limited number of breast cancer subtypes and reliance on primarily static imaging uptake measures. Future studies should examine a wider range of breast cancer subtypes as well as other glutaminolytic cancers, and validate the T/B marker with kinetic analysis of [^{18}F]4F-Gln uptake. Of note, in considering clinical translation of this method, tumors with high *GLS* activities exhibited low [^{18}F]4F-Gln PET signals (Figs. 4E and 5B) and, as such, might be mistaken for an absence of tumor. However, a robust FDG uptake was observed in the TNBC model (Fig. 4F) as well as in TNBC patients (32). Therefore, a paired FDG PET scan could guide interpretation of [^{18}F]4F-Gln PET.

Taken together, the current study provides a foundation for future studies to explore the utility of [^{18}F]4F-Gln PET in human breast cancers and other tumor types. These early results support the need for additional studies that examine the kinetics of[^{18}F]4F-Gln and the T/B index in response to a range of doses and exposure periods of *GLS* inhibitors. Such studies could firmly establish [^{18}F]4F-Gln PET–derived tracer uptake measures as predictive and PD markers for *GLS*-targeted therapy.

Disclosure of Potential Conflicts of Interest

No potential conflicts of interest were disclosed.

Authors' Contributions

Conception and design: R. Zhou, A.R. Pantel, B.P. Lieberman, H.F. Kung, D.A. Mankoff

Development of methodology: R. Zhou, A.R. Pantel, S. Li, B.P. Lieberman, H. Choi, H. Lee, H.F. Kung, R.H. Mach, D.A. Mankoff

Acquisition of data (provided animals, acquired and managed patients, provided facilities, etc.): R. Zhou, S. Li, H. Choi, E. Blankemeyer, H. Lee, R.H. Mach

Analysis and interpretation of data (e.g., statistical analysis, biostatistics, computational analysis): R. Zhou, A.R. Pantel, S. Li, H. Choi, H.F. Kung, D.A. Mankoff

Writing, review, and/or revision of the manuscript: R. Zhou, A.R. Pantel, S. Li, K. Ploessl, H. Lee, H.F. Kung, D.A. Mankoff

Administrative, technical, or material support (i.e., reporting or organizing data, constructing databases): R. Zhou, A.R. Pantel, K. Ploessl, R.H. Mach, D.A. Mankoff

Study supervision: R. Zhou, D.A. Mankoff

Acknowledgments

We thank Calithera, Inc., for providing CB839 for this study. We are grateful to Dr. Susan Demo for insightful discussions, Dr. Suzanne Wehrli for assistance in extracts study, and Drs. Ting Liu and Seok-Rye Choi for help with the pilot study. We also acknowledge Anh Nguyen, Edward Jing, Morgan Venuti, and Connor Hoge for assisting *in vivo* studies and Helen Wang for assisting image analyses.

Grant Support

This study is supported by funding from Susan G. Komen Foundation Grant SAC140060 (D.A. Mankoff), Department of Energy Grant DE-SE0012476 (D.A. Mankoff and R.H. Mach), R21-CA-198563 (R. Zhou), and R01CA211337 (D.A. Mankoff and R. Zhou). A.R. Pantel was partially supported by T32-EB004311.

The costs of publication of this article were defrayed in part by the payment of page charges. This article must therefore be hereby marked *advertisement* in accordance with 18 U.S.C. Section 1734 solely to indicate this fact.

Received July 28, 2016; revised January 10, 2017; accepted January 12, 2017; published OnlineFirst February 15, 2017.

References

1. Gross MI, Demo SD, Dennison JB, Chen L, Chernov-Rogan T, Goyal B, et al. Antitumor activity of the glutaminase inhibitor CB-839 in triple-negative breast cancer. Mol Cancer Ther 2014;13:890–901.
2. Le A, Lane AN, Hamaker M, Bose S, Gouw A, Barbi J, et al. Glucose-independent glutamine metabolism via TCA cycling for proliferation and survival in B cells. Cell Metab 2012;15:110–21.
3. Filipp FV, Ratnikov B, De Ingeniis J, Smith JW, Osterman AL, Scott DA. Glutamine-fueled mitochondrial metabolism is decoupled from glycolysis in melanoma. Pigment Cell Melanoma Res 2012; 25:732–9.
4. DeBerardinis RJ, Mancuso A, Daikhin E, Nissim I, Yudkoff M, Wehrli S, et al. Beyond aerobic glycolysis: Transformed cells can engage in glutamine

metabolism that exceeds the requirement for protein and nucleotide synthesis. Proc Natl Acad Sci 2007;104:19345–50.
5. Wise DR, DeBerardinis RJ, Mancuso A, Sayed N, Zhang X-Y, Pfeiffer HK, et al. Myc regulates a transcriptional program that stimulates mitochondrial glutaminolysis and leads to glutamine addiction. Proc Natl Acad Sci 2008;105:18782–7.
6. Seltzer MJ, Bennett BD, Joshi AD, Gao P, Thomas AG, Ferraris DV, et al. Inhibition of glutaminase preferentially slows growth of glioma cells with mutant IDH1. Cancer Res 2010;70:8981–7
7. Son J, Lyssiotis CA, Ying H, Wang X, Hua S, Ligorio M, et al. Glutamine supports pancreatic cancer growth through a KRAS-regulated metabolic pathway. Nature 2013;496:101–5.
8. van Geldermalsen M, Wang Q, Nagarajah R, Marshall AD, Thoeng A, Gao D, et al. ASCT2/SLC1A5 controls glutamine uptake and tumour growth in triple-negative basal-like breast cancer. Oncogene 2016;35:3201–8.
9. Fan J, Kamphorst JJ, Mathew R, Chung MK, White E, Shlomi T, et al. Glutamine-driven oxidative phosphorylation is a major ATP source in transformed mammalian cells in both normoxia and hypoxia. Mol Syst Biol 2013;9:712.
10. Gameiro PA, Yang J, Metelo AM, Perez-Carro R, Baker R, Wang Z, et al. In vivo HIF-mediated reductive carboxylation is regulated by citrate levels and sensitizes VHL-deficient cells to glutamine deprivation. Cell Metab 2013;17:372–85.
11. Yuneva M, Zamboni N, Oefner P, Sachidanandam R, Lazebnik Y. Deficiency in glutamine but not glucose induces MYC-dependent apoptosis in human cells. J Cell Biol 2007;178:93–105.
12. Wang JB, Erickson JW, Fuji R, Ramachandran S, Gao P, Dinavahi R, et al. Targeting mitochondrial glutaminase activity inhibits oncogenic transformation. Cancer Cell 2010;18:207–19.
13. Robinson MM, McBryant SJ, Tsukamoto T, Rojas C, Ferraris DV, Hamilton SK, et al. Novel mechanism of inhibition of rat kidney-type glutaminase by bis-2-(5-phenylacetamido-1,2,4-thiadiazol-2-yl)ethyl sulfide (BPTES). Biochem J 2007;406:407–14.
14. Thangavelu K, Pan CQ, Karlberg T, Balaji G, Uttamchandani M, Suresh V, et al. Structural basis for the allosteric inhibitory mechanism of human kidney-type glutaminase (KGA) and its regulation by Raf-Mek-Erk signaling in cancer cell metabolism. Proc Natl Acad Sci U S A 2012;109:7705–10.
15. Elhammali A, Ippolito JE, Collins L, Crowley J, Marasa J, Piwnica-Worms D. A high-throughput fluorimetric assay for 2-hydroxyglutarate identifies Zaprinast as a glutaminase inhibitor. Cancer Discov 2014;4:828–39.
16. Korangath P, Teo WW, Sadik H, Han L, Mori N, Huijts CM, et al. Targeting glutamine metabolism in breast cancer with aminooxyacetate. Clin Cancer Res 2015;21:3263–73.
17. Harding J, Telli M, Munster P, Le M, Molineaux C, Bennett M, et al. Safety and tolerability of increasing doses of CB-839, a first-in-class, orally administered small molecule inhibitor of glutaminase, in solid tumors. J Clin Oncol 33, 2015 (suppl; abstr 2512).
18. Qu W, Zha Z, Ploessl K, Lieberman BP, Zhu L, Wise DR, et al. Synthesis of optically pure 4-Fluoro-Glutamines as potential metabolic imaging agents for tumors. J Am Chem Soc 2010;133:1122–33.
19. Lieberman BP, Ploessl K, Wang L, Qu W, Zha Z, Wise DR, et al. PET imaging of glutaminolysis in tumors by ^{18}F-(2S,4R)4-Fluoroglutamine. J Nucl Med 2011;52:1947–55.
20. Ploessl K, Wang L, Lieberman BP, Qu W, Kung HF. Comparative evaluation of ^{18}F-labeled glutamic acid and glutamine as tumor metabolic imaging agents. J Nucl Med 2012;53:1616–24.
21. Venneti S, Dunphy MP, Zhang H, Pitter KL, Zanzonico P, Campos C, et al. Glutamine-based PET imaging facilitates enhanced metabolic evaluation of gliomas in vivo. Sci Transl Med 2015;7:274ra17.
22. Li S, Schmitz A, Lee H, Mach RH. Automation of the radiosynthesis of six different ^{18}F-labeled radiotracers on the AllinOne. EJNMMI Radiopharm Chem 2016;1:15.
23. Nath K, Nelson DS, Heitjan DF, Leeper DB, Zhou R, Glickson JD. Lonidamine induces intracellular tumor acidification and ATP depletion in breast, prostate and ovarian cancer xenografts and potentiates response to doxorubicin. NMR Biomed 2015;28:281–90.
24. Surti S, Karp JS, Perkins AE, Cardi CA, Daube-Witherspoon ME, Kuhn A, et al. Imaging performance of A-PET: A small animal PET camera. IEEE Trans Med Imaging 2005;24:844–52.
25. Daube-Witherspoon ME, Matej S, Karp JS, Lewitt RM. Application of the row action maximum likelihood algorithm with spherical basis functions to clinical PET imaging. IEEE Trans Nucl Sci 2001;48:24–30.
26. Wahl RL, Jacene H, Kasamon Y, Lodge MA. From RECIST to PERCIST: Evolving considerations for PET response criteria in solid tumors. J Nucl Med 2009;50(Suppl 1):122S–50S.
27. Le Belle JE, Harris NG, Williams SR, Bhakoo KK. A comparison of cell and tissue extraction techniques using high-resolution ^{1}H-NMR spectroscopy. NMR Biomed 2002;15:37–44.
28. Pantel A, Zhou R, Lee H, Li S, Doot R, Mach R, et al. Kinetic analysis of [^{18}F](2S,4R)4-Fluoroglutamine in mouse models of breast cancer with glutaminase inhibition. Society of Nuclear Medicine and Molecular Imaging (SNMMI) Annual Conference 2016:1376.
29. Carey L, Winer E, Viale G, Cameron D, Gianni L. Triple-negative breast cancer: Disease entity or title of convenience? Nat Rev Clin Oncol 2010; 7:683–92.
30. Kung HN, Marks JR, Chi JT. Glutamine synthetase is a genetic determinant of cell type-specific glutamine independence in breast epithelia. PLoS Genet 2011;7:e1002229.
31. Timmerman LA, Holton T, Yuneva M, Louie RJ, Padro M, Daemen A, et al. Glutamine sensitivity analysis identifies the xCT antiporter as a common triple-negative breast tumor therapeutic target. Cancer Cell 2013;24: 450–65.
32. Tchou J, Sonnad S, Bergey M, Basu S, Tomaszewski J, Alavi A, et al. Degree of tumor FDG uptake correlates with proliferation index in triple negative breast cancer. Mol Imaging Biol 2010;12:657–62.